Tellus (2006), 58A, 280–292
Printed in Singapore.

TELLUS

Inertial particle approximation to solutions of the Shallow Water Equations on the rotating spherical Earth

By NATHAN PALDOR* and ANDREY SIGALOV, *Institute of Earth Sciences, The Hebrew University of Jerusalem, Edmond Safra Campus, Givat Ram, Jerusalem, 91904 Israel*

(Manuscript received 29 June 2005; in final form 4 October 2005)

ABSTRACT

The present study assesses the relationship between solutions of the mechanical problem of particle motion on the surface of a rotating sphere subject only to the gravitation force (called inertial particle motion) and the fluid dynamical problem there, described by the shallow water equations (SWE). Trajectories of fluid parcels advected by a time-dependent velocity field subject to the SWE on the sphere are computed numerically and compared to analytical formulae of inertial particle trajectories. In addition, the free surface height of an ensemble of non-interacting particles is estimated within the classical mechanics framework and compared to computed height of the SWE. The comparison between solutions of the two systems shows very good qualitative as well as quantitative agreement for times of several inertial periods in the following basic low-energy cases: inertial particle oscillations in mid-latitudes (corresponding to inertial waves in fluid dynamics) and inertial motion near the equator. Moreover, for realistic values of the reduced gravity (gH of 1 to 100 $\mathrm{m^2\,s^{-2}}$) and for time interval of 1–2 d the periods of the trajectories of fluid parcels nearly coincide with those of inertial particles. These results are obtained for a wide range of initial velocity fields and they imply that, at least for time intervals considered, the Coriolis force dominates the motion even after the pressure gradient forces become sufficiently large to affect the motion. They also highlight the fact that fluid parcels of non-linear inertial waves are subject to the same westward drift as inertial particles and provide an explanation for existence of so called 'inertial peak' in the internal oceanic wave spectrum.

1. Introduction

Two classical problems are linked in the present work. The first is the particle motion on the rotating Earth subject only to the gravitation force that was investigated in many works beginning from the early–20th-century (see Whipple, 1917; Cushman-Roisin, 1982; Paldor and Killworth, 1988; Ripa, 1997). A full solution of this problem was derived in Paldor and Sigalov (2001) by employing Hamiltonian formulation of the dynamical equations.

The second problem is the fluid dynamics problem of incompressible fluid on the rotating Earth, known as the shallow water equations (SWE). Due to their complexity, the SWE have no analytical solutions but the increase in computation power in the last decades enables numerical integration of these equations with sufficient accuracy. The two systems with properly interpreted time derivatives differ by the pressure gradient term that becomes negligibly small when gravity approaches zero. We focus in the present study on establishing a relationship between solutions of the two systems when gravity is allowed to vary as a free parameter. Despite tight relationship between equations of the systems the proximity of their solutions is not guaranteed even for near-zero gravity due to inherent non-linearity of these problems.

For completeness of presentation and unification of the various formulae that appear in different forms in literature we summarize the pertinent results from inertial particle dynamics in Appendix A.

1.1. *Unified formulation of the two problems*

The SWE that describe the dynamics of an incompressible, inviscid rotating layer of fluid extending to a height h above a flat bottom may be written in vectorial form as:

$$\frac{D\mathbf{V}}{Dt} = -f\mathbf{k} \times \mathbf{V} - g\nabla h, \tag{1}$$

$$\frac{Dh}{Dt} = -h\nabla \cdot \mathbf{V}, \tag{2}$$

where $\mathbf{V} = \mathbf{i}\,u + \mathbf{j}v$ is the horizontal velocity vector, $\mathbf{i}$ and $\mathbf{j}$ are unit vectors in eastward and northward directions, respectively, $\mathbf{k}$

*Corresponding author.
E-mail: paldor@vms.huji.ac.il
DOI: 10.1111/j.1600-0870.2006.00170.x

is a unit vector in the radial direction of the sphere (pointing outward), ∇-is the *nabla* operator, g is the gravitational acceleration (or reduced gravity when buoyancy forces reduce the planetary gravitational acceleration at interface between two layers) $f = 2\Omega \sin\varphi$ is the Coriolis parameter (where Ω is the Earth's rotation frequency). φ and λ are the latitude and longitude, respectively, and the material time-derivative in Eulerian formulation is given by

$$\frac{D}{Dt} = \frac{\partial}{\partial t} + (\mathbf{V} \cdot \nabla). \tag{3}$$

Equation (1) is the momentum equation in a rotating frame with pressure determined hydrostatically by the height of the fluid and where the contribution of rotation is the Coriolis term $-f\,\mathbf{k} \times \mathbf{V}$ on the right-hand side (RHS) of (1). Equation (2) is the continuity equation in which the height h plays the role of density.

The constant g in eq. (1) represents the hydrostatic balance between gravity and buoyancy forces in fluid that results from its density stratification. Therefore, the relevant value of the parameter g in equivalent-barotropic cases is about 100–1000 times smaller in atmosphere or ocean compared to the planetary gravitational acceleration of $9.8\,\mathrm{ms}^{-2}$.

In the rest of this paper we will treat g as a small parameter of the dimensional system, that describes an equivalent-barotropic system, where the density difference between the two layers becomes infinitely small.

On the other hand, the inertial particle motion on the rotating Earth is described by the ordinary differential equations:

$$\frac{\mathrm{d}\mathbf{V}}{\mathrm{d}t} = -f\mathbf{k} \times \mathbf{V}, \tag{4}$$

$$\frac{\mathrm{d}\mathbf{X}}{\mathrm{d}t} = \mathbf{V}, \tag{5}$$

subject to the initial conditions $\mathbf{V}(0) = \mathbf{V}_0$ and $\mathbf{X}(0) = \mathbf{X}_0$, where $\mathbf{X}(t)$ is the position vector of a particle at time t. The following considerations explain the relations of this system to the SWE.

The material derivative $\frac{D\mathbf{V}}{Dt}$ in eq. (1) according to definition (3) coincides with Lagrangian time derivative $\frac{\mathrm{d}\mathbf{V}}{\mathrm{d}t}$ along the trajectory $\mathbf{X}\,(t)$. Thus one can replace the Lagrangian time derivative $\frac{\mathrm{d}}{\mathrm{d}t}$ in (4) by $\frac{D}{Dt}$. This substitution turns the ordinary differential equation (4) into a partial differential equation that coincides with (1) when $g = 0$ and which, together with the continuity eq. (2) describe the fluid dynamics of a system that we call 'inertial particle flow'. Equation (4), therefore, describes not only a single particle motion but also the dynamics of fluid subject to SWE with $g = 0$. The system (1)–(2) together with eq. (5) in turn describe the trajectory of fluid parcel subject to the SWE with arbitrary g. These considerations yield a meaningful comparison between solutions of SWE and solutions of the inertial particle flow.

1.2. SWE as a perturbation of the inertial particle flour

System (1–2) is written in spherical λ, φ coordinates as:

$$\begin{aligned}
\frac{Du}{Dt} &= v\sin\varphi\left(2\Omega + \frac{u}{R\cos\phi}\right) - \frac{g}{R\cos\varphi}\frac{\partial h}{\partial\lambda},\\
\frac{Dv}{Dt} &= -u\sin\varphi\left(2\Omega + \frac{u}{R\cos\phi}\right) - \frac{g}{R}\frac{\partial h}{\partial\phi},\\
\frac{Dh}{Dt} &= -\frac{h}{R\cos\varphi}\left(\frac{\partial u}{\partial\lambda} + \frac{\partial}{\partial\varphi}(v\cos\varphi)\right),
\end{aligned} \tag{6}$$

where

$$\frac{D}{Dt} = \frac{\partial}{\partial t} + \frac{u}{R\cos\varphi}\frac{\partial}{\partial\lambda} + \frac{v}{R}\frac{\partial}{\partial\varphi}, \tag{7}$$

and R is Earth's radius. This system can be non-dimensionalized by scaling time on $(2\Omega)^{-1}$, horizontal length on R and height h on a scale height H (i.e. mean or maximal height): The non-dimensional form of system (6) thus becomes:

$$\begin{aligned}
\frac{Du}{Dt} &= v\sin\varphi\left(1 + \frac{u}{\cos\phi}\right) - \frac{\alpha}{\cos\varphi}\frac{\partial h}{\partial\lambda},\\
\frac{Dv}{Dt} &= -u\sin\varphi\left(1 + \frac{u}{\cos\phi}\right) - \alpha\frac{\partial h}{\partial\phi},\\
\frac{Dh}{Dt} &= -\frac{h}{\cos\varphi}\left(\frac{\partial u}{\partial\lambda} + \frac{\partial}{\partial\varphi}(v\cos\varphi)\right),
\end{aligned} \tag{8}$$

where

$$\alpha = gH/(2\Omega R)^2, \tag{9}$$

is the square of the non-dimensional speed of gravity waves and the non-dimensional operator $\frac{D}{Dt}$ is the same as in (7) but with R replaced by 1. For realistic values of g (as discussed above) the values of α are 10^{-5}–10^{-3}.

Comparing the non-dimensional system (8) with the dimensional system (6) one immediately realizes that the single parameter α in the former plays the role of g in the latter. Indeed, setting $\alpha = 0$ in the non-dimensional system is entirely equivalent to setting $g = 0$ in the dimensional system and in both cases the resulting dynamics is void of pressure gradient terms. In the $\alpha \ll 1$ case the first two equations of system (8) can be viewed as perturbation of the inertial system:

$$\begin{aligned}
\frac{Du}{Dt} &= v\sin\varphi\left(1 + \frac{u}{\cos\phi}\right),\\
\frac{Dv}{Dt} &= -u\sin\varphi\left(1 + \frac{u}{\cos\phi}\right),
\end{aligned} \tag{10}$$

which is the non-dimensional inertial particle flow.

1.3. Eulerian formulation of the particle mechanics problem

A trajectory of a single free particle is a solution of the system of ordinary differential eqs. (4) and (5). Two trajectories of this system emanating from two different initial locations with some initial velocities may intersect one another at some later time $t > 0$. Thus, as argued above, in the corresponding fluid dynamical problem the fluid parcel trajectories of the system (1) (with $g = 0$) must also intersect. However, a physically acceptable solution of a PDE can only have a single value at any point in space! Hence, the inertial particle flow described by eqs. (1–2) with $g = 0$ exists only up to the first time when two of its trajectories intersect one another. Such an intersection corresponds to the appearance of 'shock waves' in solutions of partial differential equations. In a hyperbolic system such as the SWE with $g > 0$ shocks are guaranteed to develop at some finite time but this time is greater than the time of intersection of trajectories for $g = 0$ because the pressure gradient force prevents collision between fluid parcels. The formulation of the physical problem with eqs. (1–2) is not valid beyond this time and once shocks develop the mathematical formulation of the physical problem should be modified. To sum up this point—the trajectories of system (4) can be expected to accurately reproduce smooth solutions of system (1, 2) with $g = 0$ only for finite times.

Our aim is to compare analytical solutions of the ordinary differential eqs. (4–5) to the fluid parcel trajectories that result from numerical solutions of system (6). The former system has two types of solutions: cross-equatorial motion and mid-latitude oscillations (Subsection A1 and A2) and, therefore, our results (Sections 4 and 5) are classified and presented according to these two dynamical regimes.

The short review of main analytical results related to the inertial particle system is presented in Appendix A.

2. Continuity equation in Lagrangian formulation

In the Lagrangian formulation of fluid dynamics one considers an infinite ensemble of particles that fill the entire space. The continuity equation in the Lagrangian formulation is given by (Lamb, 1945; Milne-Thomson, 1996):

$$\rho(t)\,\mathrm{d}\tau(t) = \rho(0)\,\mathrm{d}\tau(0) \tag{11}$$

where ρ is the fluid density and $d\tau$ is an infinitesimal volume.

In an incompressible fluid the density is unchanged so that volume of unit mass remains constant i.e.:

$$h(t)\,\mathrm{d}s(t) = h(0)\,\mathrm{d}s(0), \tag{12}$$

where $\mathrm{d}s(t)$, $\mathrm{d}s(0)$ are infinitesimal areas of the column of fluid and $h(t)$, $h(0)$ are its heights at time t and the initial moment. On the other hand, the transformation from $\mathrm{d}s(0)$ to $\mathrm{d}s(t)$ in spherical coordinates can be written as (see e.g. Gill, 1982):

$$\mathrm{d}s(t) = \frac{\partial(\lambda(t), \varphi(t))}{\partial(\lambda(0), \varphi(0))}\,\mathrm{d}s(0), \tag{13}$$

where $\frac{\partial(\lambda(t),\varphi(t))}{\partial(\lambda(0),\varphi(0))}$ is the Jacobian of transformation from $\lambda(0), \varphi(0)$ to $\lambda(t), \varphi(t)$.

Using eqs. (12) and (13) one obtains the important relation:

$$h(0) = h(t)\frac{\partial(\lambda(t), \varphi(t))}{\partial(\lambda(0), \varphi(0))}. \tag{14}$$

Whenever (e.g. linearized inertial flour) ($\lambda(t)$, $\varphi(t)$) can be expressed explicitly as functions of ($\lambda(0)$, $\varphi(0)$) the Jacobian of the transformation follows straightforwardly and the temporal variation in the height $h(t)$ can be easily calculated from eq. (14).

3. Numerical considerations

3.1. Computation method

Numerical solutions of system (1–2) were obtained in this study by employing the STSWM package, developed in the National Center for Atmospheric Research (NCAR) specifically for numerical studies of global scale phenomena. The STSWM package is based on a spectral algorithm in which each of the continuous differentiable functions on the sphere is expanded in a truncated series of spherical harmonics. The original partial differential equations system (1–2) are first converted into vorticity-divergence-height form, which is then expanded into a series of spherical harmonics with time-dependent coefficients. The resulting system of non-linear ordinary differential equations that determines the temporal evolution of these coefficients is then solved simply by employing a first-order explicit or implicit finite difference, method (the use of an implicit finite difference method in our problem yielded identical results). In the STSWM package the spectral method described above is modified to the 'spectral transform method' described in details in Bourke (1972) and Swarztrauber (1996). The motivation for developing this method is explained by the massive computations required for calculating the non-linear terms of SWE in wavenumber space. The basic idea of this method is to locally evaluate the non-linear terms in physical space and then transform them back into wavenumber space where the spatial derivatives are calculated. This transformation greatly enhances the performance of spectral method and also has several other advantages (e.g. accuracy, see the references listed above).

3.2. Initial conditions

The initial conditions in all the numerical experiments included in this work have a meridional wave structure of (at least) one velocity component and uniform height field. In the mid-latitude case (Section 4) the zonal velocity component is zero: $v(\lambda, \varphi, t = 0) = A\cos(n\varphi)$; $u(\lambda, \varphi, t = 0) = 0$ (note that initial fields are denoted by '$t = 0$' in the argument while initial values of Lagrangian variables by '0' only) so that the velocity field is divergent, which implies that the height h is subject to temporal changes right from the very beginning. In contrast, in the equatorial cases (Section 5) the zonal velocity component of the initial field has the meridional wave form $u(\lambda, \varphi, t = 0) = A \cos(n\varphi)$ while $v(\lambda, \varphi, t = 0) = 0$. In this case the choice of u as non-zero is important since we consider separately elliptic and hyperbolic motions that differ only by the direction of the zonal velocity. Even though the divergence of this initial velocity field is zero, the temporal changes in height h are rapid when the water parcel approaches the equator.

The wavenumber n in the initial conditions was set equal to 1 in all numerical experiments but the last one (Fig. 10) in which we compare the numerical results for $n = 1, 5, 10, 20$. The comparison demonstrates that the overall conclusions of this paper are not specific to a certain initial conditions but remain valid for a wide class of initial fields.

The initial conditions for the inertial particles are always defined by the initial velocity field at the particle's initial location.

4. Low-energy dynamics in Mid-latitudes

4.1. *Inertial particle flow—analytical solutions*

Consider eq. (6) with $g = 0$. For sufficiently low fluid velocities all non-linear terms, including the advective term $(\mathbf{V} \cdot \nabla)\mathbf{V}$ in the material derivative, are much smaller than the linear terms and can be neglected. In this case the material time-derivative is approximated by the partial derivative and the first two equations of system (6) are approximated by the linear system:

$$\frac{\partial v}{\partial t} = -f \cdot u,$$
$$\frac{\partial u}{\partial t} = f \cdot v. \tag{15}$$

In the f-plane approximation we regard the Coriolis parameter $f = 2\Omega \sin \varphi$ as a constant. Therefore, the explicit solutions of these equations on the f-plane subject to the initial condition $u(t = 0) = 0$; $v(t = 0) = v_0$ (the subscript '0' denotes the value used in the initial conditions) are:

$$u(\lambda, \varphi, t) = v_0 \sin ft,$$
$$v(\lambda, \varphi, t) = v_0 \cos ft. \tag{16}$$

This solution represents the inertial waves that are traditionally obtained as the long wave limit ($k \to 0$) of inertia-gravity (Poincare) waves (Gill, 1982). In inertial waves each component of the velocity vector field simply oscillates about its mean zero value with amplitude given by the initial speed. The fluid parcel trajectories associated with it are circles—the same circles that appear in mid-latitude particle oscillations (as in Fig. 1a but without the westward drift). These known results apply only in the linearized system and on the f-plane. The numerical calculations in the next section show that these inertial waves are also solutions of the non-linear SWE on the sphere, but the fluid parcel trajectories in this case are not closed circles.

In order to obtain the westward drift of inertial particle oscillations in the linear regime when the variation of f varies with y one simply adds the westward drift to the velocity field of eq. (16). The explicit expressions for the trajectory, $\varphi(t)$, $\lambda(t)$, that corresponds to the velocities in (16) when the zonal drift Dr_λ (see eq. A6) is added are (see Paldor, 2001):

$$\lambda(t) = \lambda(0) - \frac{v_0}{f}(\cos(ft) - 1) - Dr_\lambda t,$$
$$\varphi(t) = \varphi(0) + \frac{v_0}{f}\sin(ft). \tag{17}$$

It is obvious that the Jacobian of the transformation from $\lambda(0)$, $\varphi(0)$ to $\lambda(t)$, $\varphi(t)$ in eq. (17) equals 1.0 so that according to eq. (14) the temporal changes in $h(t)$ are second order at most, i.e. to first order

$$h(t) = h(0) \tag{18}$$

along the trajectory.

4.2. *Numerical results*

Numerical integrations of the SWE using the method outlined in Section 3.1 produce fluid parcel trajectories and streamlines that confirm the analytical considerations discussed above. A comparison between solutions of the two systems also demonstrates important relevance of inertial particle mechanics to the dynamics of fluid parcels in the observable range of gH.

Figure 2 shows the trajectories of fluid parcels that obtain from the numerical solutions of the SWE starting from the initial conditions: $v(\lambda, \varphi, t = 0) = A \cos\varphi$; $u(\lambda, \varphi, t = 0) = 0$ and $h(\lambda, \varphi, t = 0) = H =$ Constant. The parameter values used in the numerical experiments in the rest of this subsection are: $A = 11.6\,\mathrm{ms}^{-1}$ and $H = 1000\,\mathrm{m}$. It is important to note that this initial velocity field is divergent, which implies that divergence effects (that are excluded in particle mechanics) affect the evolution of the flow field right from $t = 0$. The four trajectories in Fig. 2 correspond to different values of gH indicated above the panels and result from varying the value of g only. The trajectories shown are defined as solutions of ordinary differential equation

$$\frac{\mathrm{d}X(t)}{\mathrm{d}t} = \mathbf{V}(X, t), \tag{19}$$

where $X(t)$ is the coordinate vector of the fluid parcel on the sphere at time t and $\mathbf{V}(X, t)$ is the velocity field calculated from the SWE at these coordinates at the same time. The initial coordinates of the fluid parcel are $\varphi(t = 0) = 30^\circ$, $\lambda(t = 0) = 20^\circ$ in all cases. It is obvious from panel (b) in Fig. 2 that even for $gH = 10\,\mathrm{m}^2\,\mathrm{s}^{-2}$, i.e. the observationally relevant case for the ocean or the atmosphere ($H = 1000\,\mathrm{m}$ and $g = 10^{-2}\,\mathrm{ms}^{-2}$) the trajectories of system (19) have the same shape as the trajectories of the mechanical system shown in Fig. 1. According to the

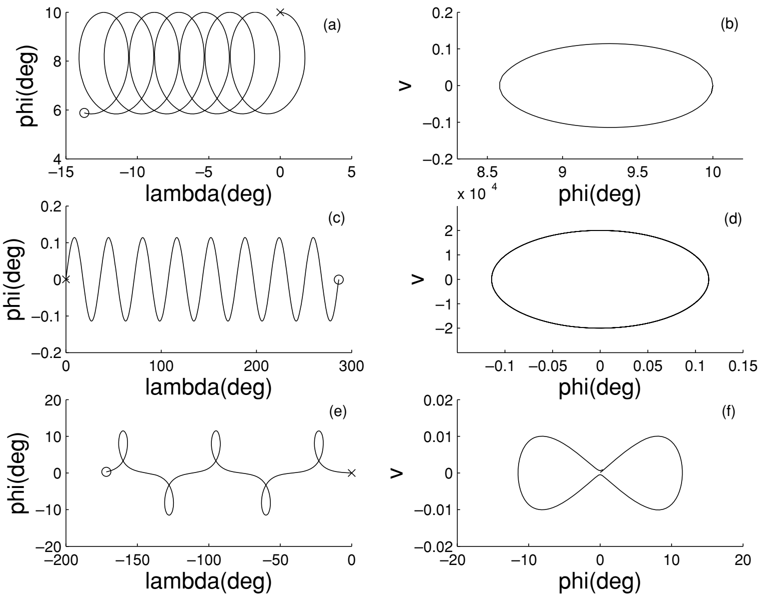

Fig. 1. The geographic, (λ, φ), trajectories (left) of the inertial particle and the corresponding phase portrait in (v, φ) phase space. The (x) marks the start of a trajectory and the circle (o) marks the end. (a), (b)—mid-latitude trajectory. $\lambda(0) = 0$, $\varphi(0) = 10^0$, $u(0) = 4.5\,\mathrm{ms}^{-1}$ and $v(0) = 0$. (c,) (d) cross-equatorial trajectory near the elliptic point. $\lambda(0) = 0$, $\varphi(0) = 0$, $u(0) = 9.3\,\mathrm{ms}^{-1}$, $v(0) = 0.2\,\mathrm{ms}^{-1}$. (f), (g) cross-equatorial trajectory near hyperbolic point. $\lambda(0) = 0$, $\varphi(0) = 0$, $u(0) = -9.3\,\mathrm{ms}^{-1}$ and $v(0) = 0.2\,\mathrm{ms}^{-1}$. The small values of $v(0)$ in the equatorial cases are required in order to insure that the particle does not remain on the equator at all times.

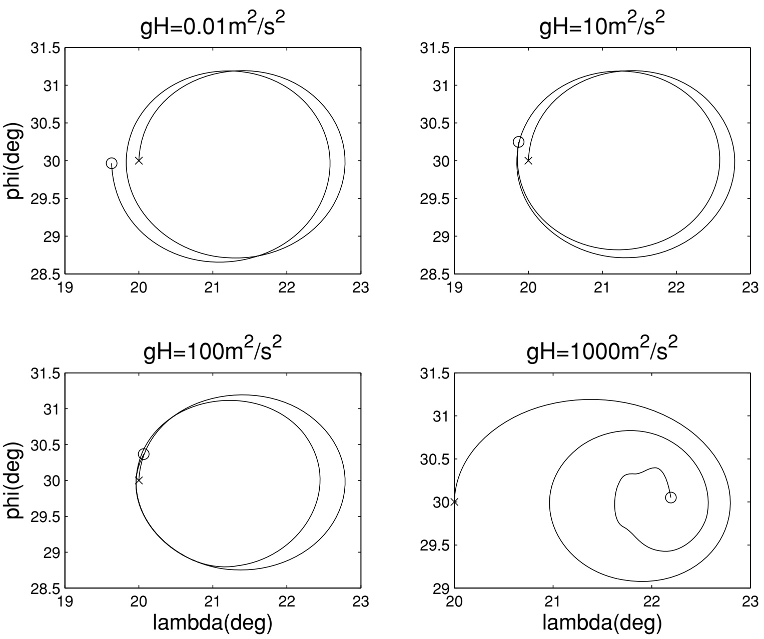

Fig. 2. Mid-latitude trajectory of a fluid parcel advected by the velocity field calculated from the SWE. The global initial velocity field is given by: $u(\lambda, \varphi, 0) = 0$ and $v(\lambda, \varphi, 0) = 11.6\cos(\varphi)$, $h(\lambda, \varphi, 0) = 1000\,\mathrm{m}$. Each of the 4 panels shows the trajectory for the indicated value of gH and all trajectories originate at $\lambda(0) = 20^\circ$, $\varphi(0) = 30^\circ$. Initial point is marked by an $\bigcirc$ and final point by an $\times$.

discussion in subsection A1 the period of these oscillations at the steady state latitude φ_s in particle mechanics is given by:

$$T_D = \frac{T}{2\sin\varphi_s}, \tag{20}$$

where $T = \frac{2\pi}{\Omega} = 24$ hr is the period of the Earth's rotation. The trajectories in Fig. 2 are all two inertial period long which, at $\varphi_s = 30^\circ$, equals 48 hr.

When these oscillations are compared to the mid-latitude oscillations of the mechanical system (top two panels of Fig. 1) one immediately notices that even for small values of gH the second cycle is already slightly distorted. At later times, the numerical calculations of the flow fields are aborted by explosive growth of all variables due to numerical instability, caused by the multivaluedness of the inviscid system, as discussed above.

A quantitative comparison between the inertial particle mechanics and the SWE obtains when one considers the period of the oscillations in the trajectories shown in Fig. 2. Although the trajectories shown in Fig. 2 for large gH are far from perfectly circular throughout the entire 48-hr trajectory, the periods of these trajectories can be calculated based on the time series of $\varphi(t)$ along the trajectory. Given our initial velocity $v(0) > 0$ (increasing latitude) and $u(0) = 0$ (so that $\varphi_s = \varphi(0)$) the period

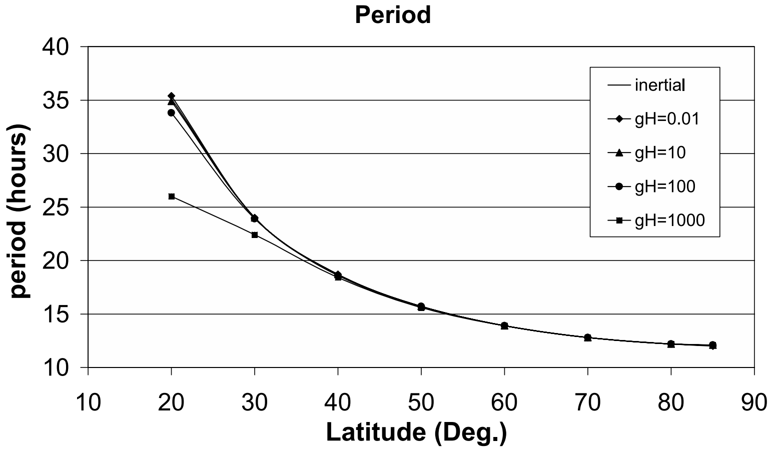

Fig. 3. The dependence of the period of a fluid parcel trajectory in mid-latitude on the initial latitude for five indicated values of gH. The period of the inertial mechanics is also shown for comparison with the particle originating from the same location as the fluid parcel and with initial velocity that equals the velocity field at the initial point. At all latitudes higher than 40° the fluid parcel period agrees very closely with the inertial period. For $g < 1$ the agreement is very good even at initial latitudes lower than 40°. Parameter values are identical with those of Fig. 2.

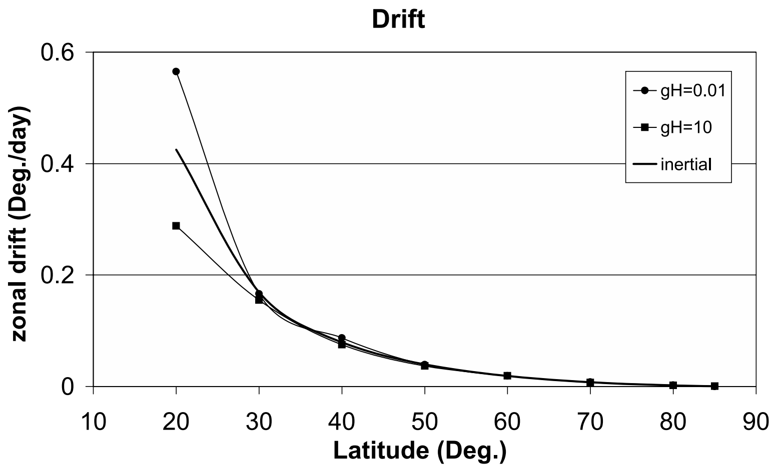

Fig. 4. The dependence of the westward drift of fluid parcel trajectory in mid-latitude on the initial latitude. At latitudes higher than 30^0 the agreement between the fluid drift and the inertial drift is good for all shown values of gH. Parameter values are identical with those of Fig. 2.

of the trajectory, T_D, was determined as the first crossing of the initial latitude from below i.e. the first t such that $\varphi(t) \geq \varphi(0)$ while $\varphi(t - \Delta t) < \varphi(0)$ (where Δt is 6 min). At $\varphi_s = 30°$ the periods calculated in this manner are impressively close to 24 hr even when the trajectory is far from circular such as for $gH = 1000\,\mathrm{ms}^{-2}$. Figure 3 shows the calculated periods of the trajectories as a function of φ_s for several values of gH along with the period of inertial particle mechanics—eq. (20). The agreement between the periods of the SWE and those of particle mechanics is impressive and for all $\varphi_s > 30°$ the difference between them is negligible even for $gH = 1000\,\mathrm{m}^2\,\mathrm{s}^{-2}$ (i.e. the $g = 1\,\mathrm{ms}^{-2}$ case).

As was mentioned earlier, the inertial circles of the particle mechanics drift westward at a rate proportional to $\frac{1}{\sin^2(\varphi_s)}$ (see equation A6). The westward drift of a fluid parcel can also be quantified by calculating the rate of change of longitude over an entire inertial period, determined by the return to the initial latitude, i.e. $\frac{\lambda(T_D)-\lambda(0)}{T_D}$ (see eq. 20). A comparison between the particle drift and the drift of fluid parcels is shown in Fig. 4 as a function of φ_s and for a few of the gH values of Fig. 2. As was the case for the period of the inertial oscillations the agreement between the particle and fluid parcel drifts is excellent for $\varphi_s > 30°$ even for the observationally relevant case of $g = 0.01\,\mathrm{ms}^{-2}$ i.e. $gH = 10\,\mathrm{m}^2\,\mathrm{s}^{-2}$. At higher gH values the fluid parcel trajectory is so strongly affected by the fast gravity waves that no estimate of the drift can be calculated from it.

Not all quantities associated with fluid dynamics have counterparts in particle mechanics. An example for such a quantity is the streamline defined by:

$$\frac{\mathrm{d}\mathbf{X}}{\mathrm{d}s} = \mathbf{V}(\mathbf{X}, t), \tag{21}$$

which at any time, t, describes a curve in $\mathbf{X} = (\lambda, \varphi)$ space that satisfies the initial conditions $\lambda(s = 0) = \lambda_0$; $\varphi(s = 0) = \varphi_0$. (Note, that although the real time, t, is a fixed parameter on the RHS of eq. (21) the parameter that actually varies along the streamline, s, has units of time as well.) Each of the four panels of Fig. 5 depicts the 24 hourly streamlines originating from = $\lambda_0 = 20°$, $\varphi_0 = 30°$ in the course of 1 d for the four values of gH employed in Fig. 2. The initial streamline in each of the four panels is obviously a straight line directed northwards by our choice of the initial velocity field. The results for $t > 0$ in all four panels clearly demonstrate that the temporal evolution of the streamline is dominated by oscillations with a 24-hr period as in the inertial particle trajectories in the vicinity of

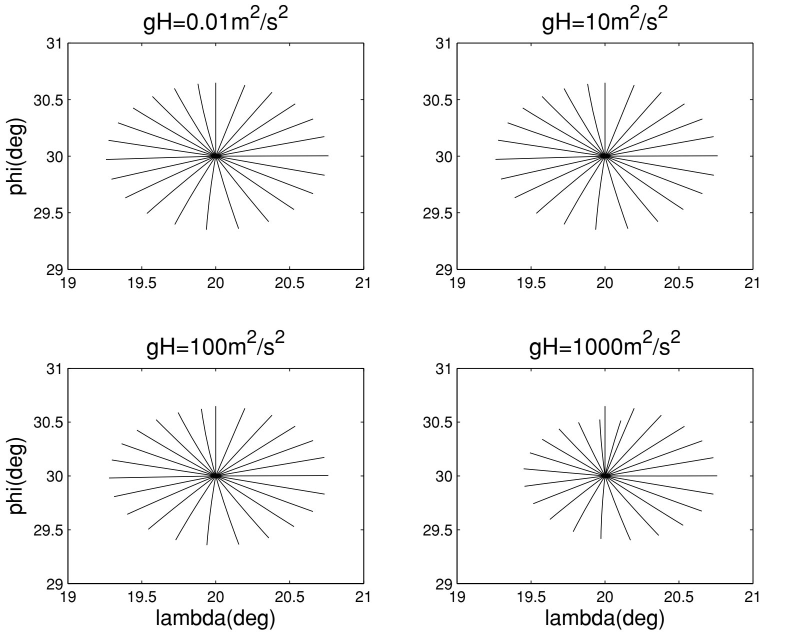

Fig. 5. Time evolution of the streamlines originating from $\lambda(0) = 20°$, $\varphi(0) = 30°$ in a low-energy velocity field. The 24 hourly streamlines on each panel cover an entire day (which is also the inertial period at 30°), the initial, $t = 0$, streamline is directed poleward (upward) and the initial fields are those of Fig. 2. All streamlines are calculated by integrating equation (21) from $s = 0$ to $s = 2$hr.

$\varphi_s = 30°$. Even for $gH = 100\,\mathrm{m}^2\,\mathrm{s}^{-2}$ the streamline goes through a complete cycle in very close to 24 hr, during which time gravity waves travel over 1000 km, so they had ample time to modify the initial velocity field substantially. As it turns out the fingerprint of inertial dynamics in the SWE is robust and gravity waves modify it only after a fairly long time.

The numerical results of mid-latitude dynamics of the SWE presented in this section point to a close link between the trajectories calculated from its velocity field and those calculated from particle inertial mechanics. On the other hand, the height field ($h(\mathbf{X}, t)$) of the SWE has no counterpart in particle mechanics but a consideration of an ensemble of particles (eq. 18) shows that $h(t)$ should not be deformed by the inertial dynamics in the mid-latitudes. However, the initial field used in the numerical calculation of the SWE trajectory ($\mathbf{V}\ (0) = (0, A \cos(\varphi))$) is divergent so that gravity waves are excited right from $t = 0$.

5. Low-energy dynamics on the equator

As is shown in Subsection A2 the motion along the equator is a steady state of the inertial system. Depending on the value of the angular momentum, D, this steady state is elliptic for $|D| > \Omega R^2$ and hyperbolic for $|D| < \Omega R^2$. It follows from eq. (A2) that on the equator $D = Ru + \Omega R^2$ so that the equatorial steady state is elliptic, if $u > 0$ on the equator and is hyperbolic if $u < 0$ there. By continuity the same is true for trajectories close to equatorial steady state: trajectories near the elliptic steady state have $u > 0$ while trajectories near the hyperbolic steady state have $u < 0$.

In accordance with the general properties of dynamical systems, trajectories near the elliptic point oscillate about the equator, reaching their maximum latitude at the point where $v = \dot{\varphi} = 0$ and from this point they move towards the equator. In contrast, trajectories near the hyperbolic points reach their minimal latitude at the point where $v = \dot{\varphi} = 0$ and from this point they move away from equator to higher latitudes. We use these properties to investigate the behaviour of inertial particles and fluid parcels emanating from a point close to equator with zero v and non-zero u.

The numerical analysis of the equatorial dynamics of the SWE we present in this section follows the above classification. In each of the two regimes we begin the analysis by drawing quantitative estimates for $h(t)$ based on the considerations presented in Section 2 that can then be compared to the numerical, fluid dynamical, results in the vicinity of elliptic and hyperbolic equatorial steady states.

5.1. Elliptic case—eastward initial zonal flow

5.1.1. Inertial particle flow—analytical solutions. If a particle is launched from $\varphi(0)$, $\lambda(0)$ with eastward directed initial velocity ($u > 0$) then the explicit expressions for the particle trajectory $\varphi(t)$, $\lambda(t)$ that solve equations (A7) are:

$$\begin{aligned} \varphi(t) &= \varphi(0)\cos(|\mu|t), \\ \lambda(t) &= \lambda(0) + \omega_D t, \end{aligned} \tag{22}$$

where μ is given by eq. (A8) (where it can be purely imaginary so its absolute value was used for clarity) and $\omega_D = \frac{D}{R^2} - \Omega$. Substituting these expressions in (14) we get:

$$h(t) = \frac{h(0)}{\cos(|\mu|t)} = h(0)\left(\frac{\varphi(0)}{\varphi(t)}\right). \quad (23)$$

This equation shows that the height $h(t)$ grows indefinitely as the trajectory approaches the equator during the first quarter of the oscillation period $\frac{1}{4}\frac{2\pi}{|\mu|}$. Hence, in contrast to the particle trajectories of Fig. 1c, a fluid trajectory may not reach the equator at all. Intuitive physical reasoning supports this result: all particles initialized near the equator on the same longitude line and with eastward directed velocity start off their trajectory by moving toward the equator. Since this is true for particles launched in both hemispheres the height (density of particles) on the equator becomes infinite when all particles converge there at $t = \frac{\pi}{2|\mu|}$. At this time, when the height on the equator as computed by the inertial mechanics becomes infinitely large, any calculation is completely irrelevant for comparison with the fluid mechanical trajectory.

5.1.2. Numerical results. These simple theoretical considerations are fully confirmed by the fluid dynamical numerical simulations. Figure 6 shows the trajectory of inertial particle (dotted curve) and the trajectories of a fluid parcel calculated with spectral algorithm (solid curve) for different values of g. Both curves have the same initial conditions: $\varphi(0) = 2^\circ$, $\lambda(0) = 20^0$ and $u(0) = 23.2\,\mathrm{ms}^{-1}$, $v(0) = 0$. The initial conditions for the SWE are: $u(\lambda, \varphi, t = 0) = A\cos\varphi$; $v(\lambda, \varphi, t = 0) = 0$ and $h(\lambda, \varphi, t = 0) = H = 1000\mathrm{m}$, $A = 23.2\,\mathrm{ms}^{-1}$. The results show an excellent agreement between the two systems even for $gH = 100\,\mathrm{m}^2\,\mathrm{s}^{-2}$.

Figure 7 compares the expression for the height $h(t)$ from particle mechanics—eq. (23) with the $h(t)$ calculated with spectral algorithm and it, too, shows a very good agreement between the two calculations.

5.2. *Hyperbolic case—westward initial zonal flow*

5.2.1. Inertial particle flow—analytical solution. In the hyperbolic case the linearized system (A7) has the explicit solution for the trajectory:

$$\varphi(t) = \varphi(0)\cosh(|\mu|t),$$
$$\lambda(t) = \lambda(0) - \Omega_D t. \quad (24)$$

The same considerations as in the elliptic case lead to the solution of eq. (14) for the height $h(t)$:

$$h(t) = \frac{h(0)}{\cosh(|\mu|t)} = h(0)\frac{\varphi(0)}{\varphi(t)}. \quad (25)$$

5.2.2. Numerical results. Let the initial conditions for inertial particles trajectory be $\varphi(0) = 0.2$, $u(0) = -23.2\,\mathrm{ms}^{-1}$, and the initial conditions for the SWE be the same as in the elliptic case except that A has an opposite sign: $A = -23.2\,\mathrm{ms}^{-1}$. These conditions guarantee that the trajectory is indeed close to equatorial hyperbolic point $v = 0, \varphi = 0, u < 0$, but do not coincide with it. (To bring it nearer to this point we decrease initial value of $\varphi(0)$ compared to the elliptic case.)

Applying the explicit solution (25) to a fluid parcel one anticipates that the height of a fluid parcel will decrease as it moves away from equator into higher latitudes. Figure 8 compares the inertial particle trajectory with its fluid parcel counterparts and Fig. 9 shows a comparison between the height calculated for an ensemble of inertial particles (25), with those of fluid parcels. As in the elliptic case, in both figures the fit between two types of curves is very good for $t < 20$ hr but the similarity breaks down when time approaches 20 hr and the height along the particle

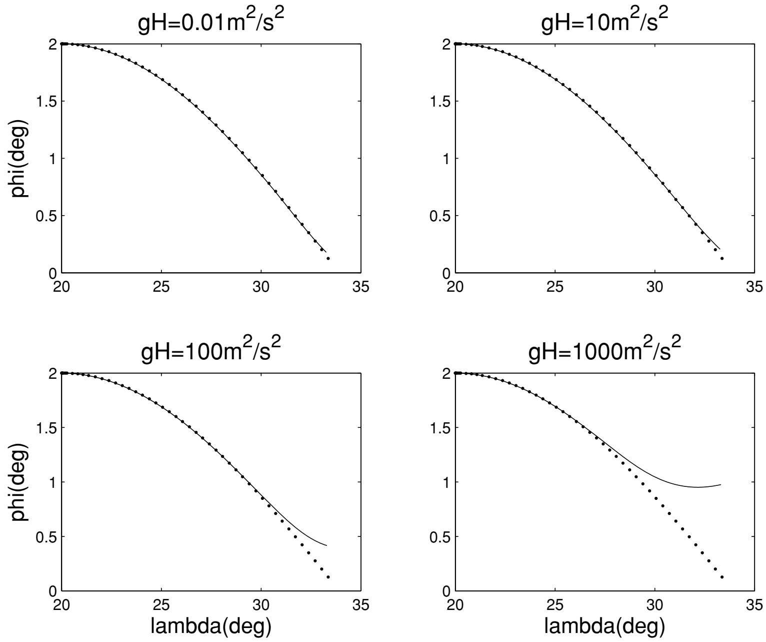

Fig. 6. The trajectory of a fluid parcel near the equatorial elliptic steady state (solid curve) and the inertial particle trajectory (dotted curve) launched with the same initial conditions as the fluid parcel. Initial coordinates: $\lambda(0) = 20^\circ$, $\varphi(0) = 2^\circ$. The initial velocity field is $u(\lambda, \varphi, 0) = 23\,\mathrm{ms}^{-1}\cos\varphi$, $v(\lambda, \varphi, 0) = 0$, and a uniform height field of 1 km. Despite the convergence of both fluid parcels and trajectories at the equator, the inertial trajectory provides a reasonable approximation to the fluid parcel trajectory for 30 hr even at $gH = 100\,\mathrm{m}^2\,\mathrm{s}^{-2}$ (i.e. $g = 0.1\,\mathrm{ms}^{-2}$). The trajectories evolve to the right and downwards relative to the launch point at the upper left corner.

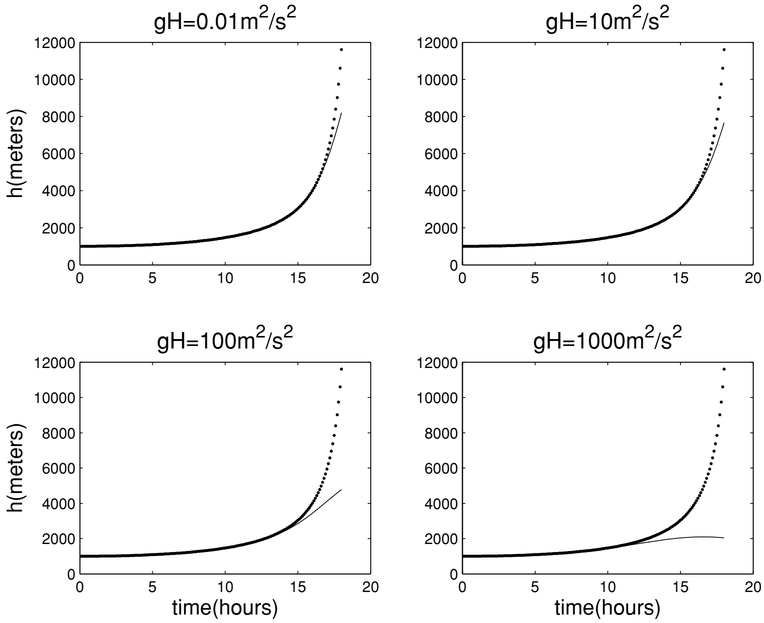

Fig. 7. Temporal variation of the height along the fluid parcel trajectory near the equatorial elliptic steady state (solid line) and the corresponding changes in height anticipated from the inertial mechanics applied to ensemble of particles (dotted line) with the same initial conditions. Initial fields and launch-coordinates of the particle and fluid parcel are the same as in Fig. 6.

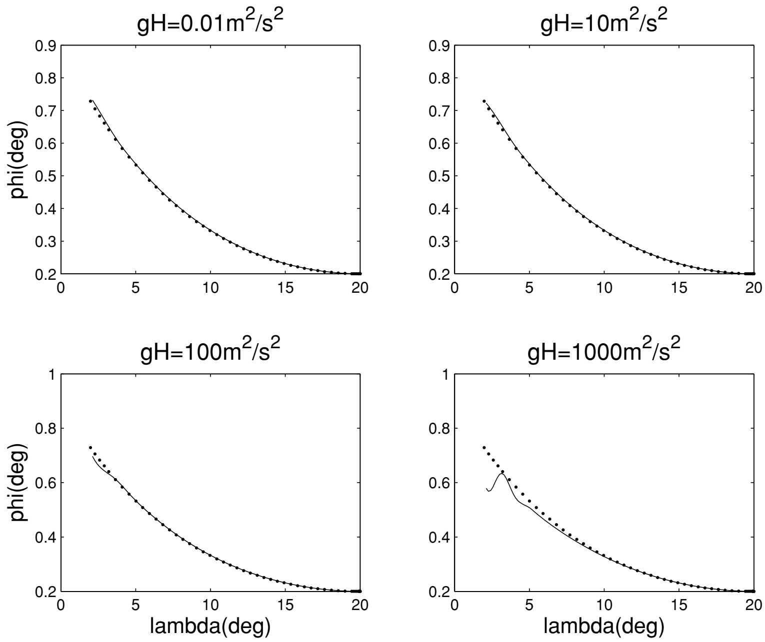

Fig. 8. The trajectory of a fluid parcel near the equatorial hyperbolic steady state (solid curve) and the corresponding inertial particle trajectory (dotted curve) with the initial fields $u(\lambda, \varphi, 0) = -23\,\mathrm{ms}^{-1}\cos\varphi$, $v(\lambda, \varphi, 0) = 0$ and $h(\lambda, \varphi, 0) = 1$ km. Initial coordinates of the trajectory: $\lambda(0) = 20^\circ$, $\varphi(0) = 0.2^\circ$. The inertial mechanics yields an accurate estimate for the fluid parcel trajectory for 20 hr even at $gH = 100\,\mathrm{m}^2\,\mathrm{s}^{-2}$. The trajectories evolve with time to the left and upwards of the launch point on the bottom right corner.

trajectory calculated from eq. (25) becomes very small so that pressure gradient forces cannot be neglected.

5.3. *Elliptic case versus hyperbolic case*

Comparing the two equatorial cases of Subsections 5.1 and 5.2 one immediately notices that for eastward initial velocity the SWE has smooth solutions for $h(t)$ and $\mathbf{V}(t)$ (solid curves in four panels of Figs. 6 and 7). In contrast, for nearly the same integration times (about 20 hr) and the same gH values, a westward initial velocity results in high frequency changes in both $h(t)$ and $\mathbf{V}(t)$ (solid curves in four panels of Figs. 8 and 9). This difference between eastward and westward initial velocity fields cannot be anticipated (or explained) based on the SWE's properties. However, the inertial mechanical considerations of Subsection A2.1 associate the smoothness of the solutions for an eastward directed initial velocity field (i.e. $u(t = 0) > 0$, $v(t = 0) = 0$) with the elliptical nature of the equator. Similarly, the erratic variations in the solutions in the case of a westward directed initial velocity (i.e. $u(t = 0) < 0, v(t = 0) = 0$) are explained by the hyperbolic nature of the equator in this case.

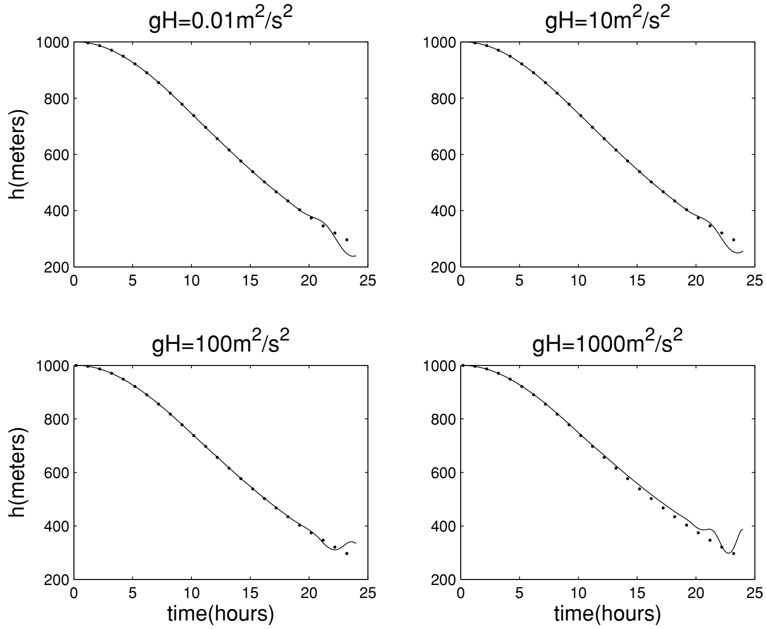

Fig. 9. The evolution of fluid parcel height near the equatorial hyperbolic steady state (solid line) and changes of height predicted for ensemble of particles (dotted line). Despite the fast (exponential) divergence the inertial mechanics yields accurate estimates for periods longer than one day. Initial fields and launch coordinates are identical with those of Fig. 8.

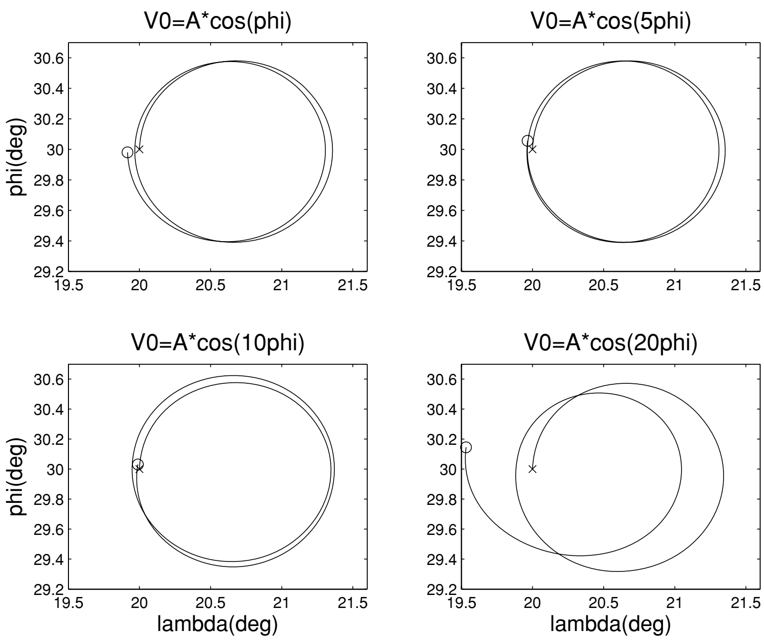

Fig. 10. Mid-latitude trajectories corresponding to the same value of g$H = 10$, but to different initial velocity fields given by: $u(\lambda, \varphi, 0) = 0$ and $v(\lambda, \varphi, 0) = A cos(n\varphi)/\cos(n\varphi(0))$, ($n = 1, 5, 10, 20,$), $h(\lambda, \varphi, 0) = 1000$ m. $\lambda(0) = 20^\circ$, $\varphi(0) = 30^\circ$. Initial point is marked by an 'x' and final point by an 'o'. Increasing wavenumber of the initial field increases initial divergense, but, as is evident from the panels parcel, trajectory keeps the spiral shape and the period.

6. Different initial velocity fields

This robustness of the inertial dynamics in mid-latitudes is not unique to the initial velocity field used in Section 4. Fig. 10 displays the effect of different initial fields on the trajectories of fluid parcels. In all panels of Fig. 10 the initial velocity field has the same divergent form: $\mathbf{V} = (0, A\cos(n\varphi)/\cos(n\pi/6))$ but the panels differ by the meridional wavenumber, n, that assumes the values 1, 5, 10 and 20. This form of the initial velocity with $A = 11.6\,\mathrm{m\,s}^{-1}$ was selected so as to ensure that in all four cases the initial velocity of the fluid parcels at $\varphi(0) = 30^\circ$ is identical while the absolute value of the divergence at that initial location increases monotonically from the upper-left panel ($n = 1$) through the upper-right and lower-left panels to the lower-right panel ($n = 20$) while in general at other latitudes the divergence is not proportional to n. The similarity between the periods of fluid parcel trajectories for $n = 1$ through $n = 20$ shows that the inertial frequency dominates the fluid parcel trajectory in the face of a 20-fold increase in the maximal initial divergence. The trajectories in Fig. 10 were calculated for $gH = 10\,\mathrm{m}^2\,\mathrm{s}^{-2}$

but similar periods were obtained when gH was increased to $1000\,\mathrm{m}^2\,\mathrm{s}^{-2}$ (the trajectories, however, are distorted more than in Fig. 10 relative to that in Fig. 1a). The results shown in Fig. 10 clearly demonstrate that the divergence of the initial field has little effect on the validity of the inertial approximation. In contrast, near the equator, where changes in $h(t)$ are $O(1)$ according to the inertial mechanics theory (i.e. either eq. 23 or eq. 25), solutions of the SWE are approximated by the inertial trajectories for less than one-quarter of the inertial period.

7. Summary and Discussion

As was mentioned in the Introduction for small g (or α) the SWE can be interpreted as perturbations to the inertial particle system. This perturbative view does not guarantee the proximity (in any sense) of solutions of the two systems subject to the same initial conditions. Nevertheless we know that such proximity of the solutions exists in the linearized shallow water theory. Indeed, the particle paths of the inertial waves solutions of linearized SWE (asymptotic long wave limit of Poincare waves) coincide with the circular trajectories of linearized inertial particle system in mid-latitude (Salmon, 1998).

It is well known that linearized equations do not always provide accurate approximations to the original non-linear system. Therefore, numerous results pertaining to linear waves in shallow water dynamics may not be applied to solutions of non-linear SWE with small non-linear terms without mathematical or numerical verification (as it is often done). The present work extends numerically the relationship between the linearized systems to the non-linear regime, where no analytical or heuristic argument exists. The zero gravity (i.e. $g = 0$) case is considered a test case for the reliability of our numerical method for solving the SWE. Trajectories of fluid parcels generated by the SWE nearly coincide with trajectories of inertial particles in this, $g = 0$, limit. For $g > 0$ the agreement between the corresponding solutions is guaranteed by continuity only for small gravity and for short times. However, just how small g should be and how short the time is for the two solutions to agree to a given accuracy is not known. It should be stressed that explicit solutions of the non-linear Eulerian SWE are not known even for $g = 0$, which is why solutions of the Lagrangian inertial particle motion were employed for comparison with the numerical solutions. Such a solution for the (Eulerian) velocity field in the $g = 0$ case is an absolute must for a formal expansion in g of the SWE, which should be the subject of a future work.

We demonstrate that the close resemblance between inertial particle trajectories and fluid parcel trajectories lasts for 1–2 d and exists for realistic values of gH in equivalent-barotropic models of the ocean or atmosphere. This resemblance is ascertained for wave-type initial velocity fields with maximum amplitude about $20\,\mathrm{ms}^{-1}$ and different wave numbers (from 1 to 20) and uniform initial height fields of 1000 m. Thus the resemblance of solutions is encountered for a broad range of initial velocity fields subject to some restrictions on their maximum values and derivatives.

The numerical results presented in this study point to the robustness of the inertial dynamics in the solutions of the SWE. Even when the fluid parcel trajectories are far from circular (e.g. the $gH = 1000\,\mathrm{m}^2\,\mathrm{s}^{-2}$ panel in Fig. 2) their period is well approximated by the inertial particle period (see the $gH = 1000$ curve in Fig. 3).

This paper also demonstrates that linear inertial waves are modified by non-linear dynamics similarly to the modification of inertial particles mid-latitude circles by β-effect. In both cases a small (i.e. $o(\beta)$) westward drift, which is easily destroyed at moderate gH values, is added to the particle or water parcel trajectory. Since the inertial period is an $O(f)$ effect, whereas the westward drift is an $o(\beta)$ effect it is not surprising that the latter is destroyed earlier than the former i.e. the period of a fluid parcel trajectory is inertial even when the parcel drifts eastwards (compare Fig. 3 with Fig. 4 for the same values of gH).

The paradigm suggested in this study, where the pressure gradient force is treated as perturbation to the inertial dynamics, differs fundamentally from the traditional approach in Geophysical Fluid Dynamics where the steady balance between pressure gradient and Coriolis forces (i.e. geostrophy) is dominant while time-dependent effects are secondary. In order for the inertial dynamics to provide sufficiently accurate solutions of the SWE it has to prevail for some finite time without generating pressure gradient forces by itself. These pressure gradient forces will be generated even for spatially uniform (i.e. non-divergent) initial velocity field. Our results in mid-latitudes show that even for the divergent initial velocity field used in Section 4 $\mathbf{V}(t = 0) = (0, v(\varphi))$, inertial particle mechanics provides an accurate approximation to solutions of the SWE for several days (inertial periods) and an ensemble of inertially moving particles does not diverge or converge there.

In contrast, on the equator where inertial mechanics predicts either convergence (23) or divergence (25) of an ensemble of inertially moving particles, the inertial dynamics provides accurate approximations to solutions of the SWE only for less than a quarter of the (longer) inertial period. This inherent limitation on the applicability of solutions of the inertial mechanical problem to solutions of the SWE exists despite the fact that in contrast to the mid-latitude case, the initial velocity field used in Section 5 is non-divergent, $\mathbf{V}(t = 0) = (u(\varphi), 0)$. Moreover, in mid-latitudes, where eq. (14) applies, during the 2 initial inertial periods gravity waves travel a distance of 1720 km or 16° for $gH = 100\,\mathrm{m}^2\,\mathrm{s}^{-2}$ so they could have easily destroyed the inertial circle whose radius at 30° is 1° only. The inertial mechanics dominates the SWE dynamics for 2 d despite the convergent initial velocity field employed in Fig. 2 where $\delta \equiv \frac{1}{R\cos\varphi}\frac{\partial}{\partial\varphi}(v\cos\varphi) = \frac{-2A\sin\varphi}{R} = -1.8\cdot 10^{-6}\ \mathrm{s}^{-1}$ for $v = A\cos\varphi$ with $A = 11.6\,\mathrm{ms}^{-1}$ at $\varphi = 30^\circ$. If this initial divergence were to last for 2 d (i.e. 172 800 s) it would have increased h by more than 30%, from 1000 m to 1300 m.

The results of this paper provide an explanation for the well known experimental phenomena in the observations of internal waves — the sharp rise of the internal wave spectrum in the neighborhood of the Coriolis frequency f, called 'inertial peak'. The 'inertial peak' contains about half of the total kinetic energy of the ocean, and even larger fraction of the mixed square vertical shear (Young and Ben Jelloul, 1997). The conclusion that can be drawn from our numerical calculations is that for a broad range of low-energy initial velocity fields and for values of the reduced gravity typical for the ocean the SWE solutions are very close to inertial waves. These solutions, obviously provide the energy that forms the 'inertial peak'.

The last point we wish to make is that despite its limitation to specific velocity initial fields, the analysis and corresponding numerical calculations presented in this study provide an important test case for numerical algorithms that strive to solve global scale fluid dynamical problems. Indeed for $gH = 0.01\,\mathrm{m^2\,s^{-2}}$ (which is the smallest value for finite gH considered in this paper) the quality and quantity characteristics of inertial particle trajectory coincide with those of fluid parcel trajectory both qualitatively and quantitatively. Thus the inertial particle motion are indeed the complementary test case suggested by Williamson et al. (1992) and an acceptable numerical package for solving the SWE on a sphere should recover these trajectories for sufficiently small g (recall that for $g = 0$ the agreement between the two is guaranteed according to the theoretical arguments given in the Introduction) at least for about two inertial periods in mid-latitudes and for nearly 1 d near the equator.

8. Acknowledgment

The comments of two anonymous reviewers helped us clarify the subtle issues addressed in this study. This research was supported by the Israel Science Foundation grant No. 579/05 to HU.

9. Appendix A: Inertial particle mechanics on the rotating Earth

In spherical coordinates eqs. (4–5) become:

$$\begin{aligned}
\frac{\mathrm{d}\varphi}{\mathrm{d}t} &= \frac{v}{R},\\
\frac{\mathrm{d}v}{\mathrm{d}t} &= -u\sin\varphi\left(2\Omega + \frac{u}{R\cos\varphi}\right),\\
\frac{\mathrm{d}\lambda}{\mathrm{d}t} &= \frac{u}{R\cos\varphi},\\
\frac{\mathrm{d}u}{\mathrm{d}t} &= v\sin\varphi\left(2\Omega + \frac{u}{R\cos\varphi}\right).
\end{aligned} \tag{A1}$$

This set of non-linear ordinary differential equations possesses solutions that can be expressed in elliptic functions (see Paldor and Sigalov, 2001). Linearizing system (A1) near its steady states yields explicit expressions for $\varphi(t)$ and $\lambda(t)$. In principle, these explicit expressions can then by substituted into the Lagrangian form of the continuity equation to obtain an explicit expression for the height $h(t)$.

The analysis of the linearized system is simplified by expressing the zonal velocity u, in system (A1) in terms of the angular momentum

$$D = R\cos\varphi(\Omega R\cos\varphi + u). \tag{A2}$$

The resulting equations in terms of D are (see, Dvorkin and Paldor, 1999):

$$\begin{aligned}
\frac{\mathrm{d}\varphi}{\mathrm{d}t} &= \frac{v}{R},\\
\frac{\mathrm{d}v}{\mathrm{d}t} &= \frac{\sin 2\varphi}{2}R\left(\Omega^2 - \frac{D^2}{(R\cos\varphi)^4}\right),\\
\frac{\mathrm{d}\lambda}{\mathrm{d}t} &= \frac{D}{(R\cos\varphi)^2} - \Omega,\\
\frac{\mathrm{d}D}{\mathrm{d}t} &= 0.
\end{aligned} \tag{A3}$$

In this system the angular momentum D is an integral of motion i.e. it plays the role of a system parameter. The dynamics described by system (A3) is different for $D > \Omega R^2$ and $D < \Omega R^2$ and depends on whether the range of latitudes visited by $\varphi(t)$ does or does not include the equator ($\varphi = 0$) at some time $t > 0$. The various dynamical scenarios that occur in the two regimes are now detailed separately.

A1. Mid-latitude

For any value of $D < \Omega R^2$ system (A3) has a steady state at $v_s = 0$, φ_s that satisfies $\cos^2\varphi_s = \frac{D}{\Omega R^2}$ and arbitrary λ. Linearizing system (A3) near this steady state one obtains:

$$\begin{aligned}
\frac{\mathrm{d}^2(\varphi - \varphi_s)}{\mathrm{d}^2 t} &= -(2\Omega\sin\varphi_s)^2(\varphi - \varphi_s),\\
\cos\varphi_s\frac{\mathrm{d}\lambda}{\mathrm{d}t} &= (2\Omega\sin\varphi_s)(\varphi - \varphi_s),
\end{aligned} \tag{A4}$$

which has the eigenvalues:

$$\mu = \pm i2\Omega\sin\varphi_s = \pm i f_s. \tag{A5}$$

Since both eigenvalues are purely imaginary this steady state is elliptic i.e. the solutions (called inertial circles) merely oscillate near it with the inertial frequency, $f_s = 2\Omega\sin\varphi_s$.

These inertial oscillations on the Earth (that describe a circle in λ, φ when the variation of f with φ is ignored) are accompanied by a slow westward drift due to the change in the Coriolis parameter with latitude. The rate of this westward drift of the inertial oscillations is given by (see: Paldor, 2001; Paldor and Sigalov, 2001):

$$Dr_\lambda = -\frac{E}{2(\Omega R^2 - D)} = \frac{-E}{2\Omega R^2\sin^2\varphi_s}, \tag{A6}$$

where $E = \frac{1}{2}v^2 + \frac{1}{2}u^2$ is the particle's (kinetic) energy. Typical numerical solutions of the mid-latitude oscillations are shown in the two upper panels of Fig. 1. Panel (b) clearly demonstrates the elliptical nature of the steady state that shows up as an ellipse in the (φ, v) phase-plane portrait. Panel (a) confirms that the motion in (λ, φ) consists of a primarily circular motion and a slow westward drift (decreasing λ).

A2. *Equator*

A simplified set that describes the particle motion near the equator is obtained by linearizing system (A3) near $\varphi = 0$ (i.e. setting $\sin\varphi \approx \varphi$ and $\cos\varphi = 1$, so that $D = (\Omega R + u)$), which results in the system:

$$\frac{d^2\varphi}{dt^2} = \left(\Omega^2 - \frac{D^2}{R^4}\right)\varphi,$$
$$\frac{d\lambda}{dt} = \frac{D}{R^2} - \Omega. \tag{A7}$$

The eigenvalues of the first equation in (A7) near the $\varphi_s = 0$ steady state are:

$$\mu = \pm\sqrt{\Omega^2 - \frac{D^2}{R^4}}. \tag{A8}$$

According to eq. (A8) the equatorial steady state is elliptic (i.e. stable) for $|D| > \Omega R^2$ (the eigenvalues are imaginary) and hyperbolic (unstable) for $|D| < \Omega R^2$ (the eigenvalues are real).

A2.1. *Elliptic case.* In this case $D > \Omega R^2$, and the first equation in system (A7) has two basic solutions:

$$\varphi(t) = \varphi(0)e^{\pm i|\mu|t} \tag{A9}$$

with μ given by eq. (A8).

It is clear that since $u = R\cos\varphi\frac{d\lambda}{dt} > 0$ (implied by $\frac{D}{R^2} > \Omega$ in the second equation of the system A7) the particle trajectory is directed eastward at all times. Since this fixed point is elliptic, small deviations from $\varphi = 0$ lead to oscillations of the solution near the equator. The oscillatory motion in (φ, v) described by the first equation in system (A7) is accompanied by a uniform eastward-directed motion along the equator with velocity $u = \frac{D}{R} - \Omega R$. Both the oscillatory motion in (φ, v) and the nearly eastward motion in the geographic, (λ, φ), plane are clearly illustrated in panels (c) and (d) of Fig. 1.

A2.2. *Hyperbolic case.* In this case $|D| < R^2\,\Omega$ so that according to eq. (A7) the zonal velocity component, u, is negative on the equator. The eigenvalues of the linearized dynamics as defined by eq. (A8) are real, and the two basic solutions are, therefore, given by:

$$\varphi(t) = \varphi(0)e^{\pm|\mu|t} \tag{A10}$$

with μ given by eq. (A8). A general trajectory is described by a linear combination of these two basic solutions: one that increases exponentially with t and the second that decreases exponentially with t. Therefore, a slight perturbation of φ from $\varphi = 0$ causes the particle to move away from the equator along the exponentially growing solution, at least for some finite $t > 0$. At longer times the trajectory may either be a mid-latitude circle of the type described in Subsection A1 (whose circular shape is distorted along its segment nearest to the equator) that remains in one hemisphere at all times or an equator crossing trajectory (of the type described in the preceding subsection but with $u < 0$ at $\varphi = 0$). More details on this issue are given in (Paldor and Sigalov, 2001). The numerical simulations in panels (f) and (g) of Fig. 1 demonstrate the hyperbolic nature of the equator in this case in both (φ, v) phase space and (λ, φ) geographic plan.

References

Bourke, W. 1972. An efficient, one-level, primitive-equation spectral model. *Mon. Weather Rev.* **100**, 683–689.

Cushman-Roisin, B. 1982. Motion of a free particle on a β−plane. *Geophys. Astrophys. Fluid Dyn.* **22**, 85–102.

Dvorkin, Y. and Paldor, N. 1999. Analytical consideration of Lagrangian cross-equatorial flow. *J. Atmos. Sci.* **56**, 1229–1237.

Gill, A. E. 1982. *Atmosphere-ocean Dynamics*. Academic Press, San Diego, 667 pp.

Holton, J. 1992. *An introduction to dynamic meteorology.* Academic Press, San Diego, 511 pp.

Lamb, H. 1945. *Hydrodynamics, sixth edition*. Dover Publications, Inc., NY, 738 pp.

Milne-Thomson, L. M. 1996. *Theoretical hydrodynamics*. Dover Publications Inc., NY, 743 pp.

Paldor, N. 2001. The zonal drift associated with time-dependent particle motion on the earth. *Q. J. Roy. Meteor. Soc.* **127**, 2435–2450.

Paldor, N. and Killworth, P. D. 1988. Inertial trajectories on a rotating earth. *J. Atmos. Sci.* **45**, 4013–4919.

Paldor, N. and Sigalov, A. 2001. The mechanics of inertial motion on the earth and on a rotating sphere. *Physica D* **160**, 29–53.

Ripa, P. 1997. Inertial oscillations and the β-plane approximation. *J. Phys. Oceaogr.* **27**, 633–647.

Salmon, R. 1998. *Lectures on Geophysical Fluid Dynamics*. Oxford University Press, 378 pp.

Swarztrauber, P. N. 1996. Spectral Transform Methods for Solving the Shallow-Water Equations on the sphere. *Mon. Wea. Rev.* **124**, 731–744.

Whipple, F. J. W. 1917. The motion of a particle on the surface of a smooth rotating globe. *Philos. Mag. J. Sci.* **33**, 457–471.

Williamson, D. L., Drake, J. B., Hack, J. J., Jakob, R. and Swarztrauber, P. N. 1992. A standard test set for numerical approximations to the shallow water equations in spherical geometry. *J. Comp. Phys.* **102**, 211–224.

Young, W. R. and Ben Jelloul, M. 1997. Propagation of near-inertial oscillations through a geostrophic front. *J. Mar. Res.* **55**, 735–766.